Measurement 227 (2024) 114194

Contents lists available at ScienceDirect

Measurement

journal homepage: www.elsevier.com/locate/measurement

Assessing the spatial distribution of positional error associated to dense point cloud measurements using regional Gaussian random fields

Yunfan Wang [a], Sofia Catalucci [b], Nicola Senin [c,b], Samanta Piano [b,*]

[a] Key Laboratory of Precision Opto-mechatronics Technology, Ministry of Education, School of Instrumentation and Optoelectronic Engineering, Beihang University, Beijing, China
[b] Manufacturing Metrology Team, Faculty of Engineering, University of Nottingham, UK
[c] Department of Engineering, University of Perugia, Perugia, Italy

ARTICLE INFO

Keywords:
Point positional error
Gaussian random fields
Local covariance
Optical coordinate metrology

ABSTRACT

Being able to assess the amount of uncertainty locally associated to dense point clouds generated by measurement can help investigate the relations between the metrological performance of a chosen measuring technology, and the local geometric and surface properties of the measurand geometry. In previous research it was demonstrated that spatial statistics based on Gaussian Random Fields and measurement repeats could be used to obtain spatial maps capturing both local dispersion and local bias associated to the position of points within measured clouds. However, the previous method had scalability limitations when handling very dense point clouds, due to it requiring the resolution of a global, increasingly larger, covariance matrix in order to solve the random field fitting problem. This work presents a variant to the previous method, where the covariance matrix is solved only locally, making the method better scalable to handle denser point clouds. Despite the new method not being able to return an equally rich information content in relation to spatial covariance, it still allows to obtain almost equally accurate information on local bias and variance, with significant gains in terms of processing speed and, importantly, making it now possible to handle very dense clouds which would be unviable to process with the original method.

1. Introduction

Uncertainty in measurement is defined by the International Vocabulary of Metrology (VIM) as a "non-negative parameter characterising the dispersion of the quantity values being attributed to a measurand" [1]. As all measurements are prone to errors, both random and systematic, a measurement result is considered complete when it is accompanied by a quantitative statement of its uncertainty. Numerous approaches to the estimation of measurement uncertainty have been established in the International Standards, including the Guide to the Expression of Uncertainty in Measurement (GUM) [2], which defines three main methods for measurement uncertainty evaluation: the aggregation of errors assessed from first principles [3,4]; the "substitution method" where uncertainty is quantified by comparing the measurement to a similar one performed on a reference object (ISO 15530 part 3 [5]); and "task-specific" uncertainty simulation, where "virtual" coordinate measuring systems are created (ISO 15530 part 4 [6]). Whereas these methods have been mainly applied in tactile measurements for decades, as optical sensors become more and more popular in industry, researchers in metrology have recently devoted themselves to investigating solutions for uncertainty evaluation in non-contact measurement [7].

A sizeable portion of scientific literature on measurement uncertainty, however, deals with the problem of evaluating uncertainty associated to a scalar measurement result: a temperature, a time interval or, in case of dimensional measurement, a length, a distance, a diameter, etc. Whilst such an approach is definitely useful to qualify measurement performance in the context of their actual application (i.e., inspection), it may fall short if the goal of uncertainty evaluation is to act as means to gain further insight on how a measuring system interacts with a measurand, and thus to understand why a specific measurement technology performs more or less poorly, when paired with a specific measurand geometry, or material, or surface. A length, diameter, distance, area or volume result – all scalar values to which uncertainty results are commonly associated – originate from a complex pipeline of data acquisition and processing steps, which – in coordinate metrology – as a

* Corresponding author.
E-mail address: Samanta.Piano@nottingham.ac.uk (S. Piano).

https://doi.org/10.1016/j.measurement.2024.114194
Received 24 March 2023; Received in revised form 17 January 2024; Accepted 18 January 2024
Available online 24 January 2024

minimum imply generation and processing of one or multiple point clouds.

Having point clouds such a central role, even more so for optical technologies where much denser clouds are typically generated, it makes sense for the literature on measurement uncertainty to invest in gaining a better understanding of the mechanisms of point cloud generation and later, point cloud processing. Mathematical models have been developed to describe the measurement systems employed in the data acquisition process (virtual instruments - for example for fringe projection [8], photogrammetry [9], laser line scanning [10], coherence scanning interferometry [11]). The main hurdle of any approach based on capturing the measurement system being the challenge of capturing the complexity of the physics interaction and obtaining a comprehensive view of all the involved error sources. In parallel, other research has specifically focused on how to model uncertainty associated to measured point clouds. Kortaberria et al. [12] proposed a method based on task-specific uncertainty assessment applied to dense point clouds in the absence of simulation models for optical systems. Forbes [13] presented a method for the estimation of uncertainty in 3D point clouds associated with their position, size and shape. As comprehensively reviewed in [14], the idea of using random variables to describe the coordinates of each point has been widely explored. Extensive work has been carried out considering positional uncertainty defined as a 3D error ellipsoid around each point in a point cloud [15–19], whereas other works proposed point positional uncertainty expressed as a one-dimensional model [20,21]. Li et al. [22] proposed an uncertainty model based on the Gaussian Mixture Model (GMM) to represent 3D point clouds and tackled registration of real-time measurements by constructing a probabilistic graph assigning each pose to a Gaussian component.

A further subject of research is studying how uncertainty propagates through any point cloud data processing pipeline (involving tasks such as point cloud simplification, segmentation, registration, fitting, etc). Forbes et al. [23,24] investigated the relationship between measurement uncertainty and fitting. Maken et al. [25] proposed a probabilistic iterative closest point (ICP) method able to capture some sources of uncertainty in point cloud registration, specifically the uncertainty of ICP's transformation parameters. Bhandary et al. [26] evaluated three uncertainty quantification methods for semantic segmentation of 3D point clouds using deep learning. Yang et al. [27] investigated 3D point cloud registration uncertainty in gap measurements using laser scanning in the context of aircraft wing assembly, studying the effects and influences of the uncertainty component generated by registration on high precision assembly and gap measurements.

Within the aforementioned state of the literature, in previous work [21] we focused on a very specific research task: develop a statistical modelling method that, starting from actual measured point clouds acquired from a real measurand geometry, could estimate local bias and/or local dispersion expected to be associated to the coordinates of the points belonging to the cloud.

The method was based on acquiring multiple point clouds with the measurement instrument of choice (usually an optical instrument), operating in repeatability or reproducibility conditions (the clouds being referred to as measurement repeats). After geometric (rigid) registration with respect to a nominal copy of the measurand geometry (e.g., a CAD model), the clouds would be used to fit a Gaussian random field (GRF), spatially wrapped around the geometry, whose local variance (measured orthogonally to the local measurand surface) would then be used as an indication of local dispersion. Local bias would be obtained as a subsequent step, by registering the fitted GRF with a further Gaussian random field obtained by fitting additional clouds belonging to a nominally more accurate instrument (for example, a CMM equipped with a traceable touch trigger probe). The final statistical model, featuring both dispersion and bias of the cloud, locally mapped to the features of the measurand geometry, would be primarily used to investigate the interactions between chosen measurement instrument/technology and local measurand shape/material/surface characteristics.

Using Monte Carlo simulation, the method would also optionally allow to study how point positional uncertainty (estimated by the GRF) would propagate to scalar linear dimensions (lengths, diameters, etc.) obtained by processing the point cloud itself. However, clearly, as discussed in the original article [21], such an estimation could not be confused with a comprehensive evaluation of an uncertainty budget, as the method would only keep into account specific error-related behaviours within the point cloud, whilst neglecting many other error sources which should be also included in a comprehensive uncertainty evaluation.

The main limitation of the method proposed in [21] was its scalability to increasingly larger/denser point clouds. In fact, fitting the Gaussian random field would require solving an increasingly larger, global covariance matrix, a task which would quickly become intractable when processing some of the larger datasets obtainable using optical measurement. For this reason, in this work we document a variant of the method proposed in [21], that allows for the covariance matrix to be estimated only locally (hence, the name of "regional" GRF, used in this work). Although approaches to the local estimation of random fields have been presented in the literature, for example based on fitting variograms, often in relation to Kriging interpolation [28–30], and in general on Gaussian processes [31,32], to our knowledge, this is the first example of presenting such an approach in the context of modelling measurement error associated to point clouds. Whilst in the original method [21] we would need to downsample the measured point clouds to approximately 20000–25000 points for the covariance matrix to be solvable on a normal desktop computer, with the variant proposed here we can process point clouds at their original density (millions of points). Despite a small loss in the final resulting statistical model, specifically consisting in the lack of covariance information modelling spatial dependencies between points, the new method still guarantees the estimation of all the needed local biases and variances, useful to study the interaction of measurement instruments/technologies with specific geometric features within the measurand geometry, and is still useful to estimate bias and variance associated to any scalar dimension obtained by point cloud processing. This latter result, though not representative of a full uncertainty budget, still allows to gain significant insight on the nature of the error associated to dimensional metrology results.

2. Methodology

2.1. Gaussian random fields for point cloud positional uncertainty

Differently from literature approaches where positional uncertainty is defined as a 3D error ellipsoid around each point in a point cloud [15–19], in this work we consider point positional uncertainty expressed as a one-dimensional displacement directed along the normal vector to the local measurand surface [20,21]. As illustrated in Fig. 1, the dispersion of each i^{th} point $\boldsymbol{p}_i$ (from measurement repeats) is projected onto the surface normal $\boldsymbol{n}_i$, where a scalar random variable z_i with reference origin $\boldsymbol{o}_i$ is used to describe the dispersion along the normal direction. Assuming z_i is from a univariate Gaussian distribution, then all the random variables construct a discrete Gaussian Random Field (GRF), and the vector field formed by the normal vectors can help to map this scalar field to the 3D Cartesian space. The approach proposed in [21] builds the GRF on the entire point cloud. It consists of N variables $\{z_1, z_2, \cdots, z_N\}$, where N is the total number of points in the cloud. The GRF is fully defined by a multivariate normal joint probability distribution with mean vector $\boldsymbol{\mu}$ and covariance matrix $\boldsymbol{K}$. However, as previously mentioned, for highly dense point clouds of millions of points, the size of the covariance matrix results in millions-by-millions values, which heavily affects the time and the computational memory for the processing of the data [33].

To avoid dealing with estimating a large covariance matrix, this work proposes the fitting of GRFs to happen locally, since the subset of a

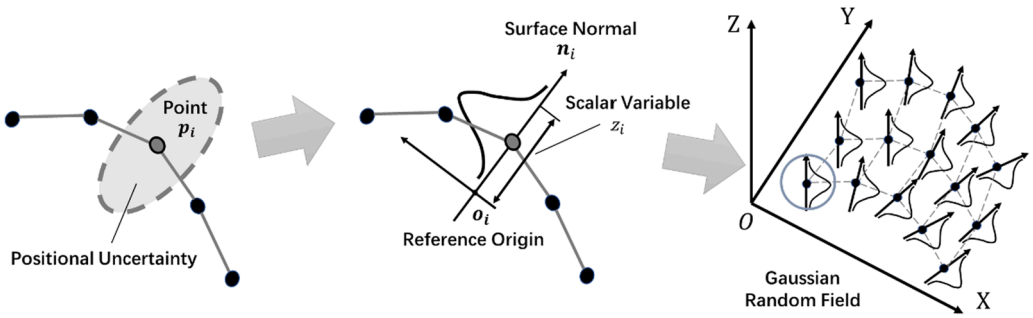

Fig. 1. The i^{th} measured point p_i is associated with its positional uncertainty. The positional dispersion in 3D Cartesian space can be projected to its normal vector, and described by a scalar random variable z_i relative to a reference origin o_i. Assuming the distribution of all random variables is Gaussian, then the discrete GRF is Gaussian. .
Adapted from [21]

multivariate normal distribution is also Gaussian. Instead of considering the covariance of the whole point cloud, the proposed method builds local or regional GRFs (identified from this point onwards as rGRFs to distinguish them from those of the previous method) that only include covariances of the point comprised within the region centred around the reference point. This is based on the assumption that spatial dependencies between measured points will only extend up to a predefined distance. As a result, the covariances between each point and its spatially closer neighbours are significantly larger than those between points that are far from the selected centre point. Fig. 2 shows how for each point it is possible to build a rGRF. For the i^{th} point p_i and its neighbouring points, the dimension of random variables is reduced to N_i, where N_i is the number of points within the selected region. The rGRF model shrinks the scale problem, significantly improving the computational efficiency.

2.2. Resampling of repeated measurements with ray casting

The first step to build the rGRF model $\{z_1, z_2, \cdots, z_N\}$ is to retrieve the observations of the random variable $z_i (i \in \{1, \cdots, N\})$ for each point. Assuming that there are R repeated measurements, for the i^{th} random variable z_i, samples $\{z_{i1}, z_{i2} \cdots, z_{iR}\}$ computed from the real measurements are needed for the construction of the rGRF. Since point clouds are unstructured (i.e. the points are stored with no information concerning their potential topological connectivity [14]), and points belonging to the individual clouds are not necessarily aligned with each other, we first need to make sure the R repeated clouds are co-localised (i.e., expressed within the same coordinate system), and then resampled at predefined locations (so that we have R observations for reach random variable z_i). To achieve this, the measurement repeats are firstly registered to the computer-aided design (CAD) model using the ICP algorithm [34,35]; then, one of the repeated measurements is arbitrarily chosen as resampling reference that defines the local coordinates of the univariate random variables. The only effect of choosing one repeat over the others as a resampling reference is in the determination of the surface locations at which the variables of the GRF model will be located. Previous experimentations [21] indicated that the influence of choosing one repeat as reference versus another is negligible, except for sharp corners where a change of location may affect the selection of the local normal used for resampling in the GRF. In the proposed procedure, the choice of one of the clouds as localisation and orientation reference introduces an element of arbitrariness, although as seen in our previous work the effect is often minimal. Resampling and interpolation are performed using a fast ray (normal vector)-triangle (mesh) intersection algorithm [36] also known as ray-casting as illustrated in Fig. 3(a). The CAD model is converted into a triangulated mesh where each triangle facet is used to determine the local unit normal vector at each point in the reference point cloud. In this work, the first point cloud is selected as the reference, and the other repeats are resampled based on the same point density and interpolated along the normal vectors to the points of the reference. For each point, the reference origins can be set as the intersection of the normal vector at the query point in the reference point cloud and the closest facet on the CAD model. The resulting intersections define the origin points to which the local values of each random

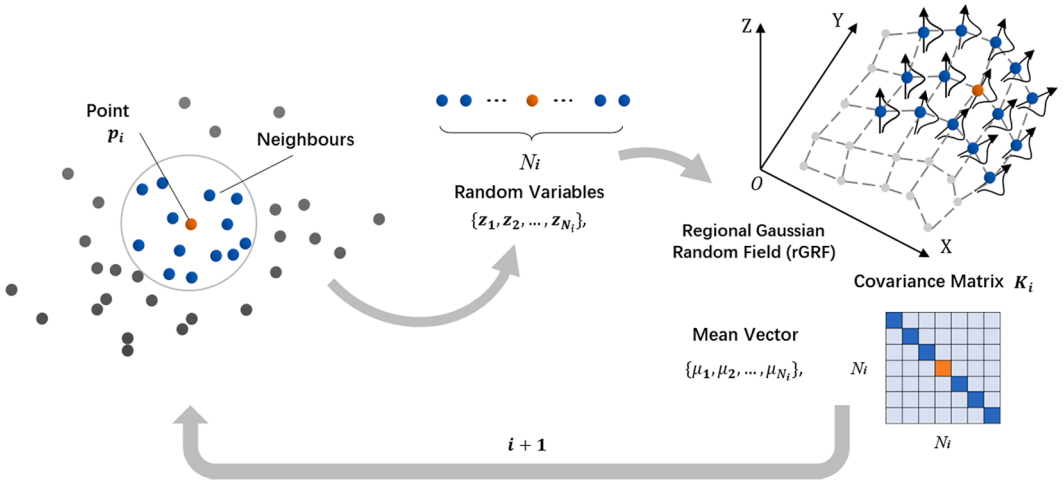

Fig. 2. The rGRF only includes the i^{th} measured point p_i (in orange) and its neighbours (in blue). The dimension of random variables N_i is reduced to the number of points within this region.

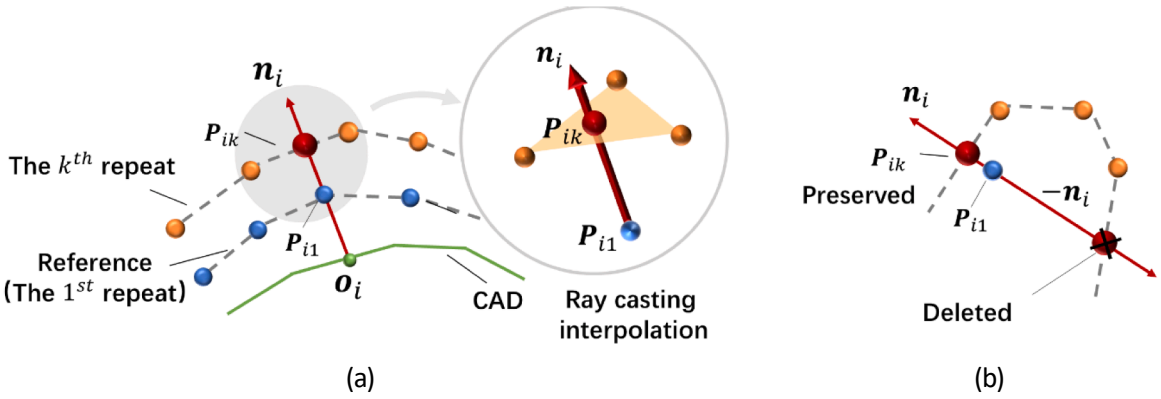

Fig. 3. The interpolation is done using a fast ray (normal vector)-triangle (mesh) intersection algorithm (ray casting). (a) All the repeats are firstly aligned with the CAD model (in green) and triangulated. For a given reference point $\boldsymbol{p}_{i1}$ (in blue) and surface normal $\boldsymbol{n}_i$, the interpolation point (in red) is the intersection with the ray defined by its normal and the closest facet. (b) The ray casting is bidirectional, therefore only the closest is kept whereas the other interpolation is deleted (identified with a black cross).

variable are referred. For a given point $\boldsymbol{p}_{ik}$ in the k^{th} repeat (where k is equal to 1 for the first repeat used as reference in this work), a bidirectional ray defined by its surface normal is used to find the closest facet and its intersection. The intersection point is the interpolation point. The same procedure can be also performed to find the reference origin $\boldsymbol{o}_i$ using the CAD mesh. Given that the normal $\boldsymbol{n}_i$ is a unit vector, then the scalar z_{ik} can be calculated as

$$z_{ik} = \boldsymbol{o}_i\boldsymbol{p}_{ik} \bullet \boldsymbol{n}_i, k \in \{1, \cdots, R\}, i \in \{1, \cdots, N\} \tag{1}$$

where R is the number of repeats, N is the number of points in the reference point cloud. The sample mean of the i^{th} random variable is calculated as

$$\bar{z}_i = \frac{\sum_{k=1}^{R} z_{ik}}{R} \tag{2}$$

which is then used as the estimator for the population mean μ_i in the vector $\boldsymbol{\mu}$.

It should be noted that bidirectional ray-triangle intersection is necessary because the repeated measured point can either be located above the reference measurement or below. However, for some cases, the ray casted from the reference point (i.e., observation viewpoint) along the direction of the normal vector intersects the surface multiple times. In this case as shown in Fig. 3(b), two intersections might be found and only the closest intersection to the viewpoint must be kept. If no intersection is found, the reference point will be eliminated. This case will happen when the ray-triangle intersection algorithm fails.

2.3. Fitting of regional GRFs

For fitting the rGRF at each point, the closest neighbouring points, that are laying on the same measurand surface, must be retrieved in order to perform the computation of the local covariance matrix. However, unlike in two-dimensional images, or any other dataset where topological information is maintained, neighbouring information is not stored in point clouds (as they are unstructured sets), so neighbours must be retrieved by solely relying on Euclidean distance, although there is the underlying risk to end up including points measured from different surfaces. Here we adopt the k-nearest neighbour (kNN) algorithm to locate the neighbouring points needed for the covariance estimation [37]. The kNN algorithm finds the k closest neighbouring points to a query point based on Euclidean distance. To partially reduce the risk of including unwanted points belonging to nearby surfaces, we implement two additional filters:

- the first filter eliminates points located beyond a predefined distance threshold from the reference point (Fig. 4(a)). This step is needed because the k-NN, instructed to retrieve k points, may end up including unwanted points located too far away if there are not enough points in the surrounding of the reference point. This filter is controlled by the threshold parameter TH_{dist};
- the second filter eliminates points whose local normal is oriented too differently from the normal associated to the reference point (an example is shown in Fig. 4(b)). This is needed to avoid points to be considered neighbours of the current one, if they belong to different surfaces. This filter is controlled by the threshold parameter TH_{angle} (maximum angle allowed between two surface normals).

Due to the application of the two filters based on TH_{dist} and TH_{angle}, the number of valid neighbours N_i may be smaller than k. The spatial extent of the rGRF is determined by the number of its valid neighbours. It should be mentioned that the number of neighbours k, thresholds TH_{dist} and TH_{angle} are three hyper parameters needed to be set in advance. The proper parameters can be determined considering the physical size of the rGRF coverage, for example using average point-to-point spacing. For instance, threshold TH_{dist} can be set as the radius of a predefined searching sphere allowing at least k neighbours can be found within the sphere for each point, while threshold TH_{angle} is determined according to the sharpest point which ensures it has enough neighbours and does not incorporate points from other surfaces.

After the valid neighbouring points are found for each reference point, the rGRF fitting process traverses every reference point running like a “sliding window”. The random variables are computed for each reference point and the rGRF is fitted point-by-point. Then, the local covariance matrix and mean vector are found. For each point $\boldsymbol{p}_i$, its rGRF $(\boldsymbol{\mu}_i, \boldsymbol{K}_i)$ is fitted after finding the correct neighbours. For the i^{th} reference point and its rGRF, the local mean vector $\boldsymbol{\mu}_i = \{\mu_{i1}, \mu_{i2}, \cdots, \mu_{iN_i}\}$ is estimated using the sample mean $\bar{z}_i (i = 1, \cdots, N_i)$ computed as explained in Section 2.2. For the estimation of local covariance matrix $\boldsymbol{K}_i$, the sample covariance matrix $\boldsymbol{S}_i$ is firstly calculated, where each element is

$$s_{m,n} = \frac{\sum_{k=1}^{R}(z_{mk} - \bar{z}_m)(z_{nk} - \bar{z}_n)}{R}, m, n \in \{1, 2, \cdots, N_i\} \tag{3}$$

However, because the sample covariance is not a good estimator of the population covariance, oracle shrinkage [38] is applied to regularise it. Hence, the local covariance matrix $\boldsymbol{K}_i$ is estimated as

$$\boldsymbol{K}_i = (1 - \rho)\boldsymbol{S}_i + \rho\frac{Tr(\boldsymbol{S}_i)}{N_i}\mathbf{I} \tag{4}$$

where $\mathbf{I}$ is the unit matrix, $Tr()$ is the trace and factor ρ is

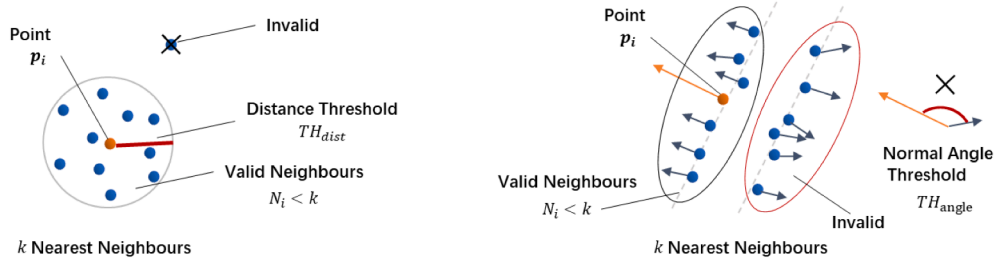

Fig. 4. Neighbour selection for rGRF fitting. (a) A very distant point (marked by a black cross) is originally included within the k-nearest neighbours of the reference point $\boldsymbol{p}_i$ (orange) but is filtered out by the distance threshold TH_{dist}. (b) A set of points originally included in the k-nearest neighbours of reference point $\boldsymbol{p}_i$ are filtered out by the angle threshold TH_{angle}, as they indeed belong to a close, but differently oriented, surface.

$$\rho = \min\left(\frac{\left(1-\frac{2}{N_i}\right)Tr\left(\boldsymbol{S}_i^2\right)+Tr^2(\boldsymbol{S}_i)}{\left(R+1-\frac{2}{N_i}\right)\left[Tr\left(\boldsymbol{S}_i^2\right)-\frac{Tr^2(\boldsymbol{S}_i)}{N_i}\right]},1\right), 0<\rho\leq 1 \tag{5}$$

2.4. Regional GRFs for variance and bias

The diagonal elements of the estimated local covariance matrices identify the variance of the points within the selected region. From this information, it is possible to create spatial models of local dispersion in the direction of the local normal (overlaid to the mean point cloud generated from the rGRF, as shown in Fig. 5). Local bias information can be also added if a more accurate reference from a traceable instrument (for example point clouds obtained from a tactile coordinate measuring machine – CMM) of stated uncertainty or a mathematical model with associated bias is available. Following the first route that using CMM data, a set of more accurate repeated measurements go through the same rGRF process, and the mean point clouds registered with the same reference CAD mesh are obtained. Then the bias is defined as the distance from the mean point cloud of the evaluated instrument to the high accuracy CMM mean point cloud (Fig. 5).

After estimating the local covariance matrix, for the i^{th} point ($i \in \{1, 2, \cdots, N\}$), a vector of standard deviations $\boldsymbol{\sigma}_i$ is extracted as

$$\boldsymbol{\sigma}_i = \sqrt{diag(\boldsymbol{K}_i)}, \tag{6}$$

where $diag()$ is the operation to extract the diagonal elements from a matrix. The mean z value of each reference point ($\bar{z}_i$) is computed using the sample mean. For the i^{th} reference point, the coordinates of the mean point $\bar{\boldsymbol{p}}_i$ are determined by

$$\bar{\boldsymbol{p}}_i = \boldsymbol{o}_i + \bar{z}_i \bullet \boldsymbol{n}_i \tag{7}$$

After the rGRF fitting is complete, the obtained model can be used to generate new virtual (local) point clouds. This step is done by first using

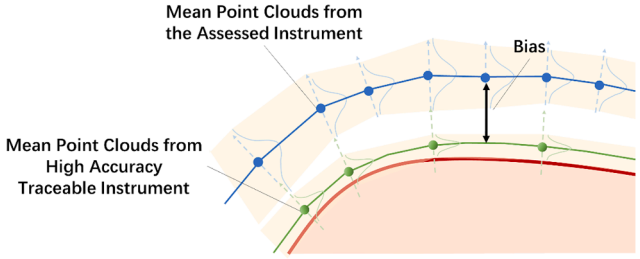

Fig. 5. In blue the mean point cloud of the assessed instrument, generated using the rGRF approach. In green the mean point cloud from the high accuracy traceable instrument, such as tactile CMM. The bias is defined as the distance between the mean point clouds extracted from the rGRFs.
Adapted from [21]

Cholesky decomposition on the local covariance matrix $\boldsymbol{K}_i$, so that a lower triangular matrix $\boldsymbol{L}_i$ is obtained. Hence,

$$\boldsymbol{K}_i = \boldsymbol{L}_i \boldsymbol{L}_i^{\mathrm{T}} \tag{8}$$

Then, a new observation vector of the current region $z_{i,new}$ is generated using

$$\boldsymbol{z}_{i,new} = \boldsymbol{\mu}_i + N(0,1)\boldsymbol{L}_i \tag{9}$$

where $\boldsymbol{\mu}_i$ is the mean vector of the current local region, $N(0,1)$ is a vector where each element is drawn from the standard normal distribution. For the i^{th} point, let $z_{i,new}$ be the new sample of the reference point extracted from the observation vector $z_{i,new}$, the new point is recovered as

$$\boldsymbol{p}_{i,new} = \boldsymbol{o}_i + \boldsymbol{z}_{i,new} \bullet \boldsymbol{n}_i \tag{10}$$

The new virtual repeats can be used in data processing for error estimation in linear dimensions, as illustrated in Fig. 6. Unlike the GRF approach presented in [21], the rGRF method does not require the covariance of the whole point cloud, and it can be performed on segmented regions of interest. The initial real repeated measurements are fed as input data. New point clouds are then generated and, for each new repeat, key linear dimensions are extracted using feature fitting. The probability distributions can be retrieved. To incorporate the bias, high accuracy traceable measurements are required, and the same procedure is performed. The bias is estimated by comparing the two obtained distributions.

3. Results

3.1. Experiment setup and artefact

A reference polymer artefact first proposed in [39] and manufactured using a HP Fusion 3D high-speed sintering (HSS) system was selected as test case. The artefact consists of a hollow, four-walled cube (edges of 40 mm) with spheres of 5 mm radius at each vertex (Fig. 7(a)). In our experimental setup, the artefact was placed at the centre of a turntable, with markers sticked onto the surface of the object to aid for automated registration of scans from different viewpoints. A fringe projection optical measuring system was used, mounted on a tripod, as shown in Fig. 7(b). Five measurements of the entire surface of the selected object were obtained using the fringe projection instrument. Three additional, repeated measurements were obtained using a tactile instrument.

The fringe projection system selected for this study was a GOM ATOS Core 300 commercial instrument. The field of view is (300 × 230) mm with measuring point distance at 0.12 mm, as provided by the manufacturer. The parameters used for the GOM are defined in the GOM Acceptance Test with reference to the Guideline VDI/VDE 2634 Part 3 [40] given by the manufacturer:

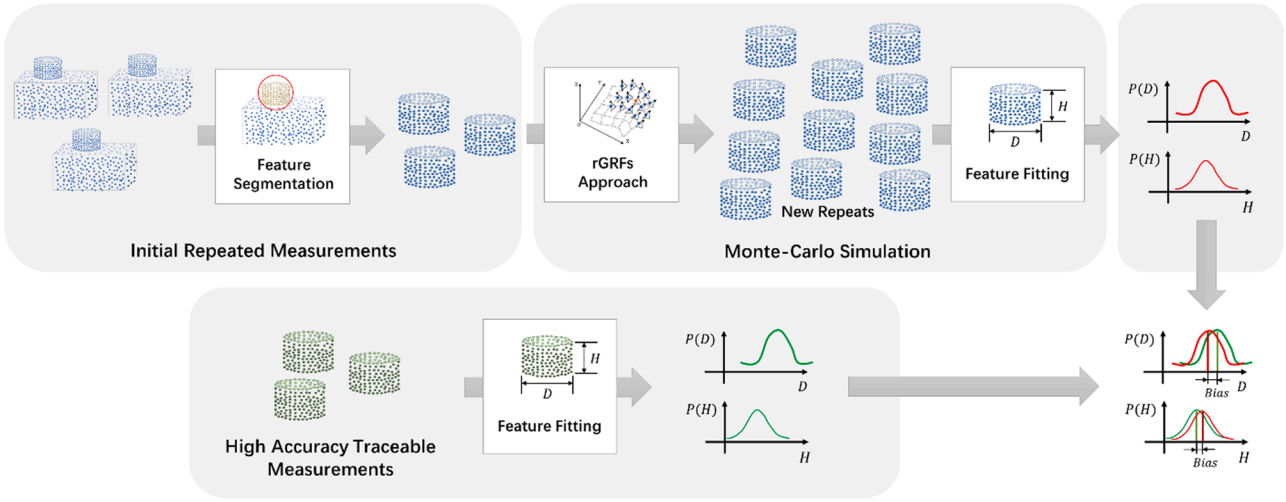

Fig. 6. Error estimation in linear dimensions extracted from segmented regions of interest in the point cloud. .
Adapted from [21]

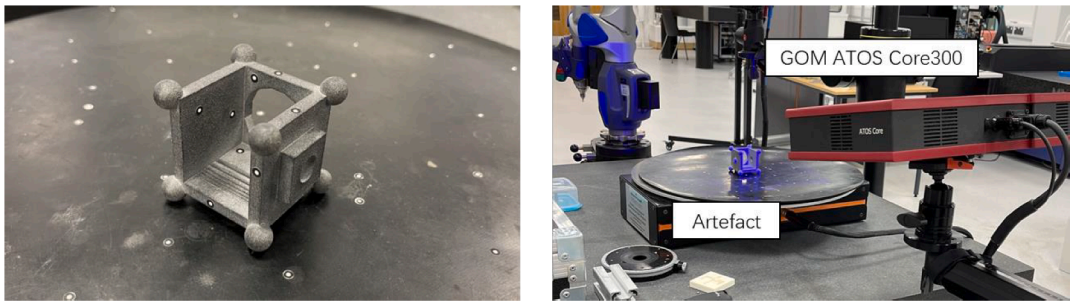

Fig. 7. Artefact and experimental setup. (a) Additively manufactured part (artefact) with sticked markers for registration of multiple measurements. (b) Artefact placed on a turntable and fringe projection system mounted on a tripod.

Probing error form (sigma) 0.006 mm
Probing error size 0.027 mm
Sphere spacing error 0.020 mm
Length measurement error 0.047 mm

The tactile CMM instrument was a Mitutoyo Crysta Apex S7106 with a 21 mm long, 5 mm diameter ball tipped stylus. The instruments are both available in the temperature-controlled at (20 ± 0.5) ℃ Manufacturing Metrology Team laboratory at the University of Nottingham.

The optical measurements with the fringe projection system resulted in five-point clouds of 4,000,000 points each. The first test was performed by application of the rGRF and original fitting [21] methods to downsampled versions of the original point clouds. Downsampling was performed using the grid average method [41], to achieve target spacing of 0.5 mm between neighbouring points. The parameter of 0.5 mm for downsampling of point clouds was chosen based on previous tests [21] to ensure a meaningful comparison between the global method and the one presented in this work, as the global fitting approach could not be applied on point clouds with very high densities as measured by the optical instrument. In this experiment, downsampling brought each cloud from 4 million to approximately 25,000 points.

Finally, to compare the performance of the new and previous methods in local bias estimation, further GRFs were obtained by fitting the CMM point cloud repeats (3 repeats). As the point clouds obtained by CMM measurement consisted of approx. 6000 points each, these point clouds were not downsampled, but instead directly used to fit the random field using both the rGRF and the original method [21]. Note that the CMM measurements covered only some selected surfaces of the artefact. Therefore, the bias maps were only obtained for those surfaces.

A second test was performed to demonstrate the computational robustness of the new method (regional GRF, referred to as rGRF in this work) by applying the method to fit a regional GRF to the original full-density measured point clouds (using an available triangle mesh of the object as reference, and adopting the hyperparameters$k = 25$, $TH_{dist} = 3.98$mm and $TH_{angle} = 45^{\circ}$ for the kNN method needed to compute the contents of the local moving window. Furthermore, the rGRF model was fitted to specific surfaces of the test artefact, aimed at estimating bias and dispersion associated to selected regions of interest.

3.2. Analysis of the results

We start by commenting the results obtained on the downsampled point clouds. Fig. 8 shows the maps of the standard deviations extracted from the GRF and the rGRF for visual comparison. In Fig. 9 the frequency histograms of the same local standard deviations are shown. Finally, in Fig. 10 the local biases are compared. Note that in Fig. 10 the local bias maps were only computed for the surfaces we had CMM data for. As it can be observed in Fig. 8 the standard deviations estimated with both methods share some visual similarities. For example, the standard deviations are larger in correspondence of sharp edges for both methods, a known modelling artefact due to possible errors in local estimation of the z reference coordinate in correspondence to sharp edges. Despite the above similarities, the standard deviation map of the rGRF appears more

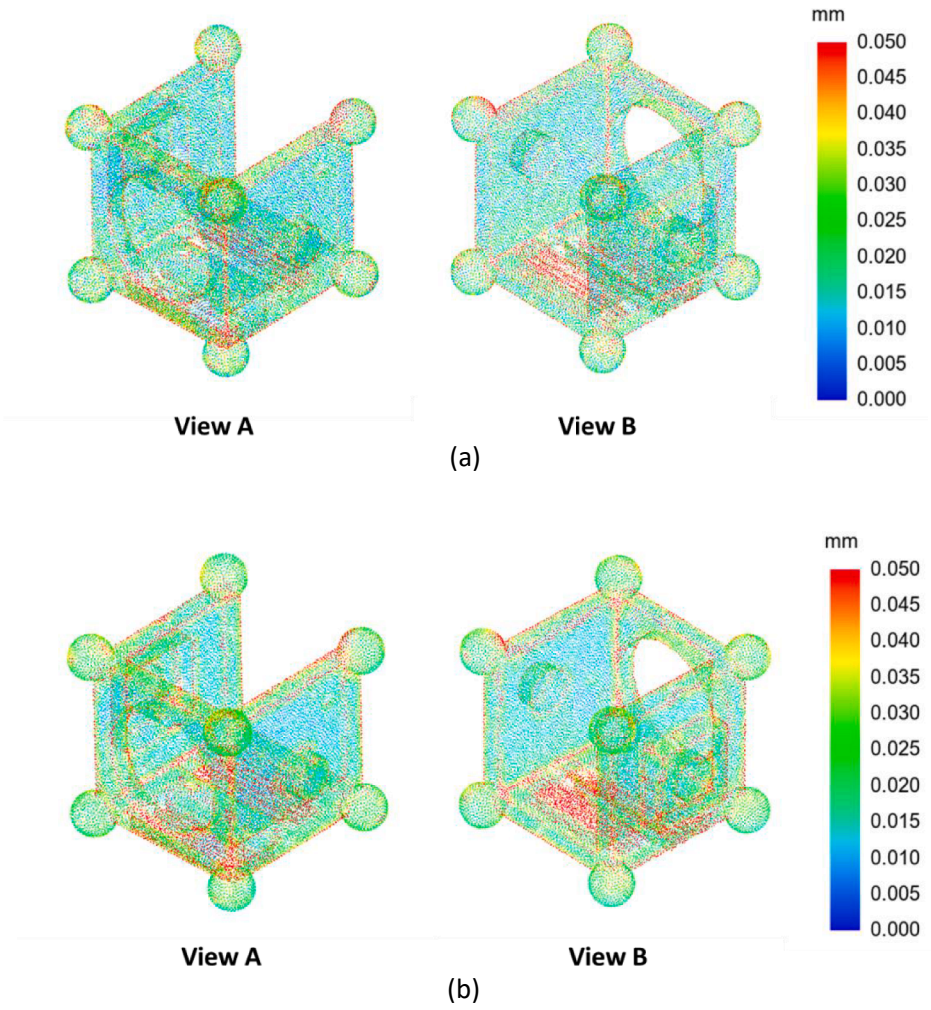

Fig. 8. Standard deviation maps. (a) GRF method proposed in [21] and (b) rGRF method proposed in this work.

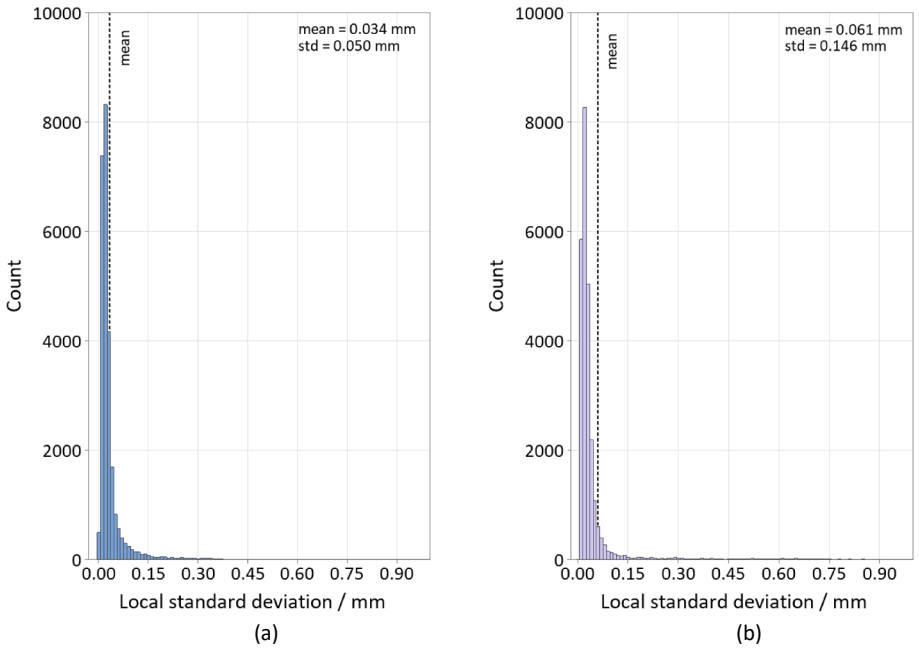

Fig. 9. Distribution of local standard deviation. (a) GRF method, (b) rGRF method.

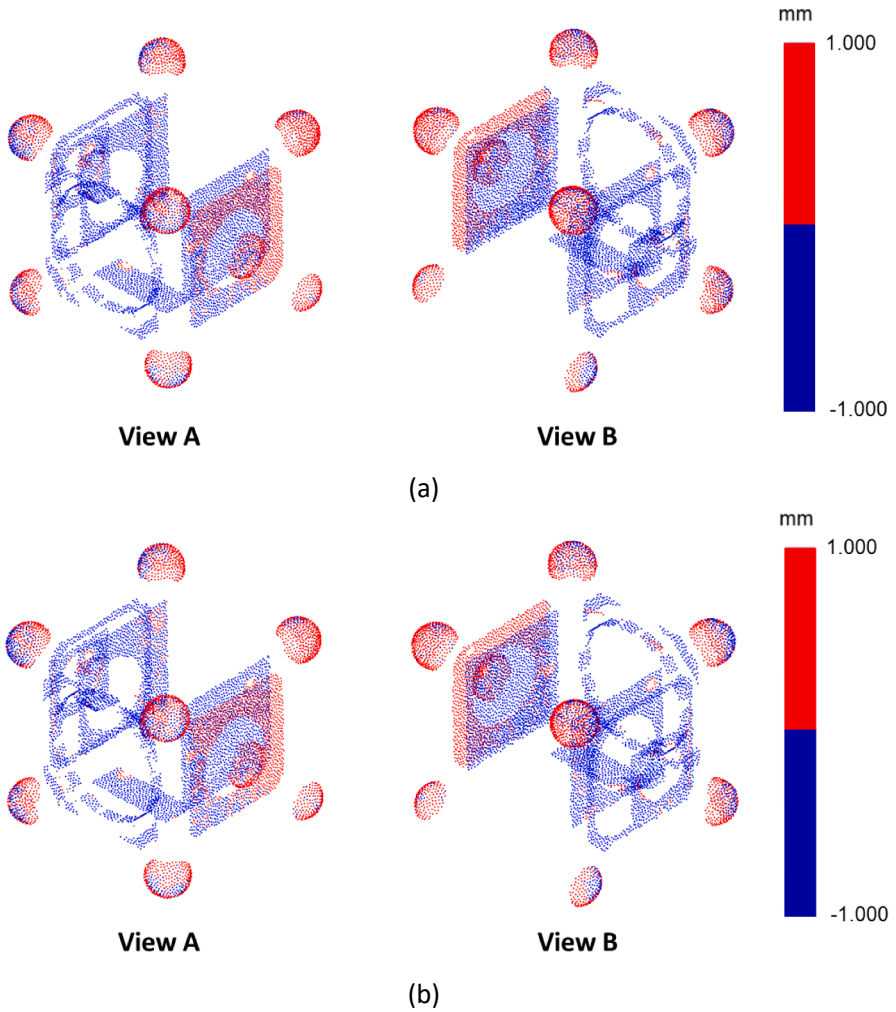

Fig. 10. Local bias maps. (a) GRF method proposed by [21] and (b) rGRF method proposed in this work.

homogeneously distributed compared to the GRF one (Fig. 8), and shows higher mean and standard deviation (Fig. 9). These differences might be caused by the local estimation of covariance performed in the rGRP (as opposed to the original method which considers the covariance of the entire point cloud). The discrepancy may also be caused by the thresholds chosen to select the points that fall within each moving window, a parameter missing in the original GRF approach. For the local bias maps (Fig. 10), the measurements appear as positively biased in correspondence of the sphere features and negatively biased for the majority of the planar features, except the one containing the cylindrical extrusion which appears as positively biased.

Fig. 11 shows the results of the standard deviation and local bias maps on highly dense measurements that global GRF approach [21] cannot process, while Fig. 12 shows the distribution of local standard deviations. For local bias, a similar behaviour to what achieved on dowsampled point clouds can be observed. For the standard deviation map, lower dispersion values can be seen in correspondence with the edges and corners compared to the subsampled results, reinforcing the interpretation of the error being mostly due to how the reference z coordinate is computed for each point of the Gaussian field, an issue common to both rGRF and GRF approaches, as they use the same method.

As stated earlier, the regional GRF method allows to separately fit individual surfaces, in order to target the study of measurement behaviour in correspondence of specific surfaces. This is possible due to the nature of the regional fitting, which takes place within a moving window whose range of allowed positions can be defined in advance. In this type of usage of the rGRF method (i.e., targeting a specific subset of surfaces), the allowed locations for the moving window can be determined by segmenting the point cloud in order to isolate the targeted surfaces. The high density point clouds can be segmented using the direction of the local normal vectors at each point computed by principal component analysis (PCA) in combination with k-means clustering [14]. The typical use of fitting rGRF to specific subsets of surfaces is to estimate bias and dispersion of dimensional results computed on such surfaces.

In Fig. 13, an example of local standard deviation maps obtained from rGRF models fitted to specific surfaces of the test artefact are shown (for example a sphere, the cylindrical inner surface of a through hole, and two planar parallel surfaces). The selection of surfaces is aimed at estimating bias and dispersion associated to the sphere diameter, cylinder diameter, and linear distance between the two planes, respectively.

3.3. Standard and expanded uncertainty on dimensions

Selected dimensions (specifically the diameter of a sphere, the diameter of an inner cylinder and the distance between two parallel planes) were computed as follows: i) the point cloud regions supporting each dimension were extracted from the original clouds using the segmentation method previously illustrated in Section 3.2; ii) these regions were individually fit to GRFs (using both the global [21] and the

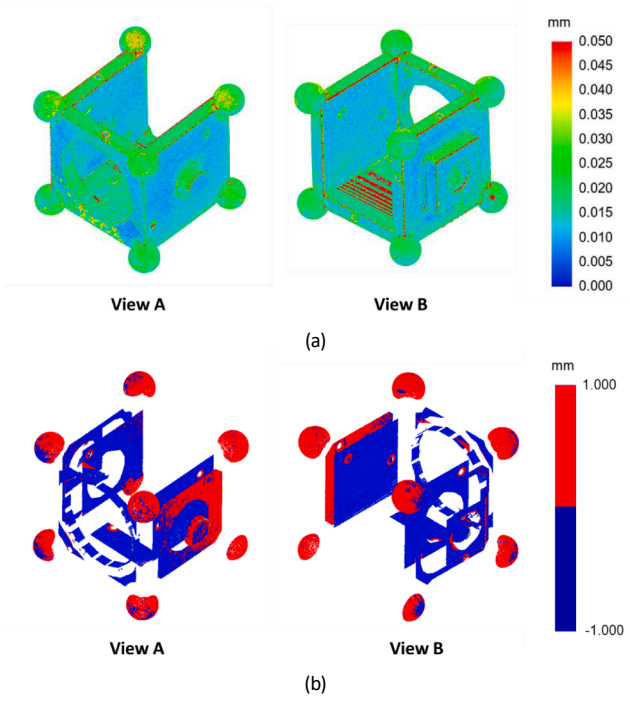

Fig. 11. Maps of the original highly dense point clouds and application of the rGRF approach. (a) Standard deviation map and (b) local bias map. The global GRF results could not be presented because the GRF method [21] cannot process a point cloud of this size.

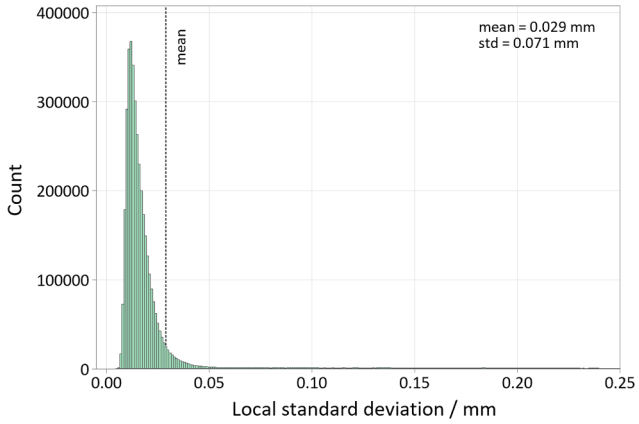

Fig. 12. Distribution of local standard deviation (original highly dense point clouds using the rGRF approach). The global GRF result could not be plotted because the GRF method [21] cannot process a point cloud of this size.

regional method); iii) (Monte Carlo simulation) 30 new clouds were generated from each GRF or rGRF, each being a new observation extracted from the random field (using the procedure illustrated in Section 2.4); iv) each new cloud was fit to an appropriate datum, needed to define the feature of size (sphere and cylinder for the diameters, planes for the linear distance (see also [21]); v) the final value for the dimension was extracted from the datum, leading to the construction of a frequency histogram of dimension values (30 values per dimension). This entire process was applied to: the original clouds, the downsampled ones, and the CMM point clouds (the latter to establish a baseline for comparing the frequency distributions).

For an unbiased measurement resulting in a scalar value and represented as a random variable X, described by n observations x_i, the standard uncertainty [42] is defined as the standard error of the mean.

Given n new observations extracted from the GRF and rGRF (where n is equal to 30 and M indicates fringe projection measurements in this work), and n results for the dimensional feature $x_1, x_2, \cdots, x_n$ computed from such point clouds generated from the GRF and rGRF, the standard uncertainty u_M is defined as

$$u_M = S_{\mu_x} = \frac{s}{\sqrt{n}} \tag{11}$$

where μ_x is the population mean, S_{μ_x} is the standard error of the mean and s is the sample standard deviation computed on the n point clouds generated from the field, i.e.

$$s = \sqrt{\frac{1}{n-1}\sum (x_i - \bar{x})^2} \tag{12}$$

The expanded uncertainty U_M is obtained by multiplying the standard uncertainty by a coverage factor k

$$U_M = k \bullet u_M \tag{13}$$

In this work, k was set to 2. in order to provide a level of confidence of approximately 95% under the assumption of X (i.e., either the sphere diameter, the cylinder diameter or the linear distance) being normally distributed.

To include the bias term, the CMM measurements (three repeats) were considered as the more accurate reference, thus:

$$\text{bias}_{X:(\text{CMM}-\text{M})} = (\bar{x}_{\text{CMM}} \pm u_{\text{CMM}}) - (\bar{x}_M \pm u_M) \tag{14}$$

where $\text{bias}_{X:(\text{CMM}-\text{M})}$ is the bias on the dimension X measured with measurement system M extracted from the point clouds generated from the field with respect to the reference CMM value ($\bar{x}_{\text{CMM}}$ is the mean of three CMM repeats). As regulated by the BS ISO 22514 part 7 [43], it is possible to rely on the maximum permissible error (MPE) specified by the manufacturer to compute the standard uncertainty $u_{\text{CMM}} = \text{MPE}/\sqrt{3}$ of the CMM, or alternatively to the manufacturer's MPE, the error E_0 reported in a recent calibration certificate can be used instead. For the CMM, we chose to use the data from our most recent calibration certificate: $E_0 = (1.7 + 3L/1000)\mu\text{m}$ (where L is the test length in millimetres). The mean value of the linear features extracted from the CMM measurements are given in Table 1, as well as the u_{CMM}.

The values for the selected dimensions, computed from the new observations extracted from the GRF and rGRF fields fitted on the downsampled point clouds, are reported in Table 2 and summarised in Fig. 14. The bias values are reported in Table 3. In the table, the label "(dense)" refers to results obtained from Gaussian fields fitted to the original high-density point clouds.

ANOVA tests for equal means performed separately on each dimension resulted in the null hypothesis (GRF, rGRF and rGRF (dense) having equal means) not being rejected at the 0.05 significance level for Ø sphere and Ø cylinder. It is possible that the observed differences in bias may become statistically significant with larger sample sizes. Conversely, for the linear distance between two planes, the ANOVA test resulted in the null hypothesis being rejected with p-value equal to 1.28×10^{-30}, meaning that the difference of biases can be considered as statistically significant (assuming a common CMM value as reference).

It is important to point out that what shown in this section is only an example to demonstrate how the GRF can be used to study the propagation of measurement error to scalar dimensions computed form the point cloud. Clearly, more accurate and comprehensive means to model the uncertainty associated to the CMM measurements could be used in our model, and these would lead to a more accurate evaluation of uncertainty in the final results. However, this would not change the proof of concept in relation to how the proposed method can be used to study error propagation. The main strength of this method is that it gives us the possibility to study "local" error (bias and dispersion) associated to the point cloud, and to study how it propagates to scalar dimensions, if desired. If the final goal is to obtain an accurate uncertainty estimation

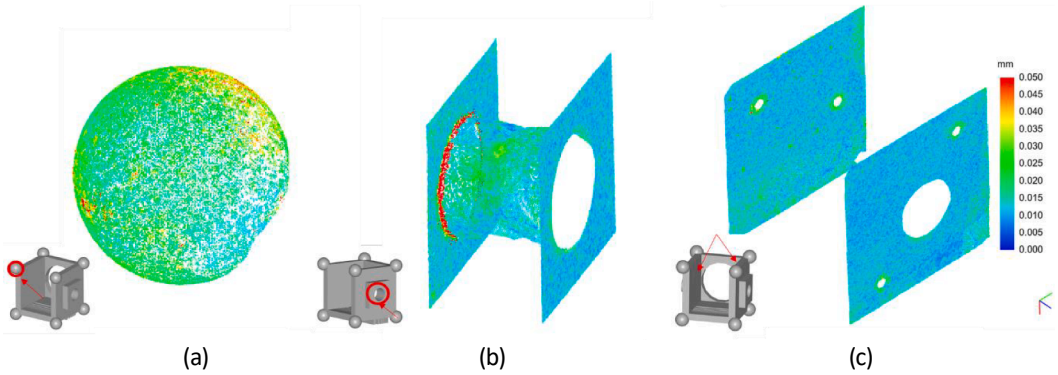

Fig. 13. The local standard deviation maps obtained on surface subsets, extracted directly from the high-density point clouds; (a) spherical surface, (b) inner cylindrical surface of a through hole, and (c) two parallel planes.

Table 1
Dimensions estimated on CMM data/mm.

Feature	Nominal value	Mean value $\bar{x}_{CMM}$	u_{CMM}
Ø sphere	10.000	9.880	0.001
Ø cylinder	10.000	10.109	0.001
d plane to plane	30.000	30.180	0.001

for measured dimensions, other approaches presented in the literature [10] and in the international standards may be more comprehensive.

4. Discussion

The use of both global GRF fitting [21] and local fitting (rGRF) presented in this work can depict the random error components of points positional uncertainty and have the flexibility to further incorporate a bias term with the help of a more accurate instrument. Using Monte Carlo simulation, both approaches can generate new observations from the fitted field. However, differently from the GRF approach shown in [21], the method presented in this work shows clear advantages in scalability when processing highly dense point clouds, allowing measurement analysis without information loss induced by cloud downsampling, necessary in the previous method [21]. In addition, due to the capability of fitting locally the rGRFs, point positional uncertainty information can be captured in correspondence to selected regions of interest in the measured part.

A direct comparison of the performances of the new rGRF method and original one was only possible when operating on downsampled point clouds. In such case, the standard deviation maps of the random fields generated by the two methods shows a similar trend in correspondence to sharp edges, estimating locally higher dispersions (compared to estimates on other geometric features). The local standard deviation estimates of the rGRF method appear spatially more homogeneous, compared to the GRF, but also feature almost doubled values. Local bias value estimates are also approximately doubled for the rGRF, although both methods generate bias maps with similar trends (paired to the same CMM contact measurement). The trend of the bias map features positive bias values for the most part in correspondence of the sphere features, and negative bias values for the majority of the planar features except for the one containing the cylindrical extrusion showing partially positive bias values. This latter exception could be caused by warping or collapsing of the printed material during or after the manufacturing process, or be the result of a registration error.

As a comparison of the GRF and rGRF methods on the point clouds at native density was not possible, our analysis consisted of verifying if the rGRF results on the lower-density point clouds would be at least approximately confirmed/replicated on the native densities. The similarities are confirmed both on the estimated bias and standard deviation maps.

As shown in the results, the confidence intervals estimated by the GRF and rGRF on the selected dimensional feature show differences, both in terms of central tendency (bias) and dispersion (standard deviation), albeit being obtained using the same reference clouds from contact measurement. The only exception is the sphere diameter showing only a few micrometres difference in standard deviation and a good consistency in bias between all the methods. For all methods, the plane-to-plane distance shows the smallest dispersion but low accuracy compared to the CMM measurements, whereas the cylindrical inner surface shows higher dispersion values in all cases but is closer to the CMM results.

For the downsampled cases, both rGRF and GRF methods present similar uncertainty estimations for the spherical surface and inner cylindrical surface cases, but the rGRF method shows the smallest bias in the latter. The expanded uncertainty of plane-to-plane distance calculated on the rGRF results is nearly one magnitude smaller than that obtained applying the GRF method. However, the calculated bias is

Table 2
Dimensions estimated from fringe projection measurements/mm.

Method	Feature	Nominal value	Mean value $\bar{x}_M$	u_M	$U_M(k=2)$
GRF	Ø sphere	10.000	9.861	0.009	0.019
rGRF			9.863	0.010	0.020
rGRF (dense)			9.865	0.011	0.022
GRF	Ø cylinder	10.000	10.067	0.042	0.085
rGRF			10.095	0.038	0.076
rGRF (dense)			10.067	0.077	0.155
GRF	*d* plane to plane	30.000	30.223	0.002	0.003
rGRF			30.252	0.0003	0.0005
rGRF (dense)			30.233	0.0001	0.0003

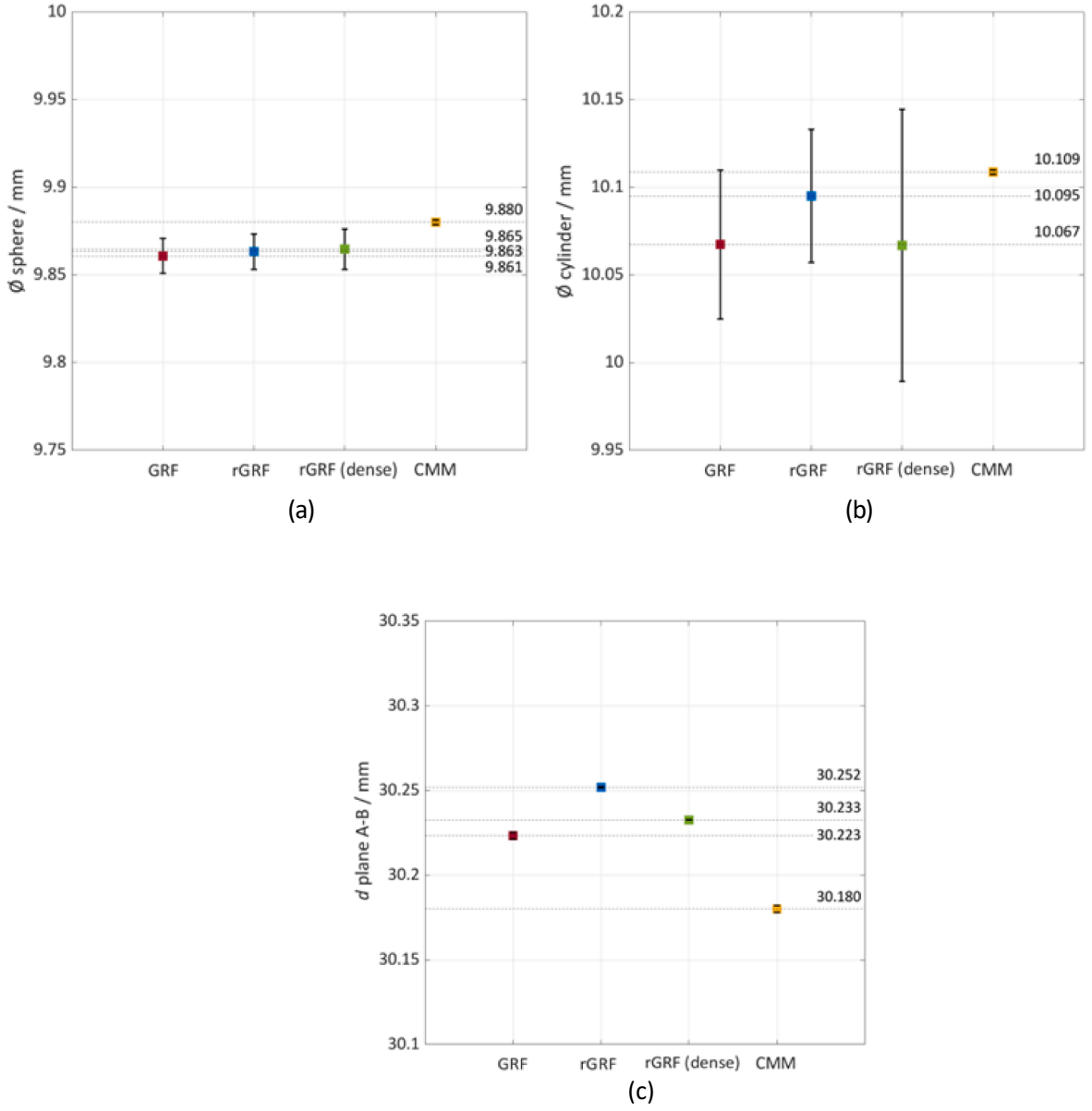

Fig. 14. Mean values and standard uncertainties for the selected dimensions ((a) sphere diameter, (b) cylinder diameter and (c) linear distance) after sampling 30 new observations from Gaussian fields (global fitting and regional fitting on full density and downsampled point clouds). The interval computed on the CMM measurements is u_{CMM} reported in Table 1.

Table 3
Bias values/mm.

Method	Feature	$bias_{x:(CMM-M)}$
GRF	Ø sphere	$(9.880 \pm 0.001) - (9.861 \pm 0.009)$
rGRF		$(9.880 \pm 0.001) - (9.863 \pm 0.010)$
rGRF (dense)		$(9.880 \pm 0.001) - (9.865 \pm 0.011)$
GRF	Ø cylinder	$(10.109 \pm 0.001) - (10.067 \pm 0.042)$
rGRF		$(10.109 \pm 0.001) - (10.095 \pm 0.038)$
rGRF (dense)		$(10.109 \pm 0.001) - (10.067 \pm 0.077)$
GRF	*d* plane to plane	$(30.180 \pm 0.001) - (30.223 \pm 0.002)$
rGRF		$(30.180 \pm 0.001) - (30.252 \pm 0.0003)$
rGRF (dense)		$(30.180 \pm 0.001) - (30.233 \pm 0.0001)$

almost double compared to the original GRF approach.

Similarities are not observed when applying the rGRF method to the feature segmentations with different density (downsampled case and native case). Although the sphere diameter again shows consistency both in terms of central tendency and dispersion, the behaviour of inner cylindrical diameter and plane-to-plane distance are different. This time, the diameter extracted from the highly dense inner cylindrical surface shows higher bias and standard deviation compared with the downsampled case. However, the plane-to-plane distance shows similar dispersion in both cases but better central tendency from the dense one.

For the inner cylindrical surface case, one possible explanation could be that the inner surfaces of the through hole and the sharp external edges are challenging to measure, especially when using optical instruments. The inner surfaces have generally lower signal-to-noise ratio (SNR) due to the presence of occlusions and shadowing, while the sharp edges may induce large interpolation error. Another consideration can be made regarding the fitting error. The measurement of the inner

cylindrical surface is incomplete due to occlusions, which can potentially affect the fitting algorithm and the consequent diameter extraction. In contrast, the sphere fitting on far more complete measurements shows higher robustness with small variations in the diameter values. A different consideration can be made for the plane-to-plane distance: the Euclidean distance from the centroid of plane 1 perpendicular to plane 2 is considered as the final result for the linear dimension. This result is surely influenced by the fitting of the two datums, especially in the case of rGRF (dense): if the points are many, the generation of new point clouds result in variances that behave as balanced noise, which added to the robustness of the fitting, leads to small dispersions.

5. Conclusions

This research proposes a computationally efficient method to fit point clouds to Gaussian random fields, useful to investigate the local effects of measurement error on acquired point clouds, regardless of the optical measurement system used and its specifications. The method (referred here as rGRF – regional Gaussian random field) builds upon previous work on fitting entire point clouds to a Gaussian random field (GRF) [21]. As opposed to the previous method, in this work we estimate the covariance matrix (needed to fit the random field) locally on moving windows that encompass a finite number of neighbouring points. As the window size is limited, the covariance matrix is easier to compute due to the reduced number of points to consider within the window. The advantage of the proposed rGRF method is that point clouds of any size (i.e., various densities) can be fitted as long as the hardware is able to support the large number of iterations needed to build the model and extract the matrix of covariance. On the contrary, the original method was not scalable to high density clouds because the covariance matrix would become too large to estimate, and cloud downsampling would become necessary. The disadvantage of the rGRF method is that, for each position of the moving window, although the entire covariance matrix is computed, only the variance of the central (reference) point in the window is kept, ultimately resulting in a Gaussian random field for the entire cloud that only captures point variances, and not covariances. Another known issue for both original and proposed method is that if the part to be measured presents very complex features, the resampling process might be affected, and the wrong interpolation and large fitting errors might cause significantly large variances. Despite the limitation, we have shown that, when the GRF and rGRF methods are compared on downsampled point clouds (so that the GRF is still applicable), the results are comparable, both in terms of describing local variance and bias of the entire field, and in terms of generating individual biases and variances for selected dimensions, needed to estimate measurement uncertainty. Additionally, we show that the rGRF can be applied to entire, high-density point clouds (where the original GRF would not be applicable), obtaining results that, despite not being confrontable with those obtained from the original method, still show consistency with the estimates on the downsampled clouds.

The developed method has the capability of processing highly dense point clouds and it is a preliminary attempt to evaluate uncertainty of dense point clouds, which is still an area of open research. Further work will involve a more thorough investigation of the factors that contribute to some of the discrepancies nevertheless observed between the new rGRF and the original GRF method in cases where direct comparison is possible (i.e., downsampled point clouds). More importantly, future investigations will look into the development of a method to retain covariances between points as the moving window -used for regional fitting- moves across the point cloud. Advanced computing techniques such as distributed computing [44] can be used to overcome memory shortage when retaining the covariances of large-scale point clouds.

CRediT authorship contribution statement

Yunfan Wang: Writing – review & editing, Writing – original draft, Validation, Methodology, Investigation, Formal analysis, Data curation. **Sofia Catalucci:** Writing – review & editing, Writing – original draft, Validation, Supervision, Methodology. **Nicola Senin:** Writing – review & editing, Writing – original draft, Supervision. **Samanta Piano:** Supervision, Resources, Investigation.

Declaration of Competing Interest

The authors declare that they have no known competing financial interests or personal relationships that could have appeared to influence the work reported in this paper.

Data availability

The authors chose not to share the data/code of this research. Some contents may be available on request

Acknowledgements

The authors would like to thank the China State Scholarship Fund (202106020154) and the UKRI Research England Development (RED) Fund via the Midlands Centre for Data-Drive Metrology for funding this work.

References

[1] BIPM, IEC, IFCC, ILAC, ISO, IUPAC, IUPAP, OIML, International Vocabulary of Metrology—Basic and General Concepts and Associated Terms (Bureau International des Poids et Mesures) JCGM 200, 2012.
[2] JCGM 100, GUM 1995 with Minor Corrections, Evaluation of Measurement Data — Guide to the Expression of Uncertainty in Measurement, BIPM, France, 2008.
[3] D. Barchiesi, T. Grosges, Propagation of uncertainties and applications in numerical modeling: tutorial, J. Opt. Soc. Am. A 34 (2017) 1602–1619, https://doi.org/10.1364/JOSAA.34.001602.
[4] H. Haitjema, Measurement uncertainty, in: R.K. Leach, S.T. Smith (Eds.), Basics of Precision Engineering, CRC Press, 2018. Chap. 9.
[5] ISO 15530 part 3, Geometrical Product Specifications (GPS) – Coordinate Measuring Machines (CMM): Technique for Determining the Uncertainty of Measurement - Part 3: Use of Calibrated Workpieces or Standards, International Organization for Standardization, 2011.
[6] ISO/TS 15530 part 4, Geometrical Product Specifications (GPS) – Coordinate Measuring Machines (CMM): Technique for Determining the Uncertainty of Measurement - Part 4: Evaluating Task-Specific Measurement Uncertainty Using Simulation, International Organization for Standardization, 2008.
[7] G. Wübbeler, M. Marschall, K. Kniel, D. Heißelmann, F. Härtig, C. Elster, GUM-compliant uncertainty evaluation using virtual experiments, Metrology 2 (1) (2022) 114–127, https://doi.org/10.3390/metrology2010008.
[8] Y. Zhao, Y. Cheng, Q. Xu, Z. Luo, X. Wang, H. Li, Uncertainty modeling and evaluation of profile measurement by structured light scanner, Meas. Sci. Technol. 33 (9) (2022) 095018.
[9] D. Sims-Waterhouse, M. Isa, S. Piano, R. Leach, Uncertainty model for a traceable stereo-photogrammetry system, Precis. Eng. 63 (2019) 1–9, https://doi.org/10.1016/j.precisioneng.2019.12.008.
[10] M. Vlaeyen, H. Haitjema, W. Dewulf, Digital twin of an optical measurement system, Sensors 21 (19) (2021) 6638.
[11] R. Su, R. Leach, Physics-based virtual coherence scanning interferometer for surface measurement, Light Adv. Manuf. 2 (2021), https://doi.org/10.37188/lam.2021.009.
[12] G. Kortaberria, U. Mutilba, S. Gomez, B. Ahmed, Three-dimensional point cloud task-specific uncertainty assessment based on ISO 15530-3 and ISO 15530-4 technical specifications and model-based definition strategy, Metrology 2 (4) (2022) 394–413, https://doi.org/10.3390/metrology2040024.
[13] A.B. Forbes, Uncertainties associated with position, size and shape for point cloud data, J. Phys. Conf. Ser. 1065 (2018) 142023, https://doi.org/10.1088/1742-6596/1065/14/142023.
[14] S. Catalucci, N. Senin, State of the art in point cloud analysis, in: R.K. Leach (Ed.), Advances in Optical Form and Coordinate Metrology, IOP Publishing, 2020. Chap. 2.
[15] M. Mezian, B. Vallet, B. Soheilian, N. Paparoditis, Uncertainty propagation for terrestrial mobile laser scanner, Int. Arch. Photogramm. Remote Sens. Spatial Inf.

Sci. XLI-B3 (2016) 331–335, https://doi.org/10.5194/isprs-archives-XLI-B3-331-2016.
[16] M. Ozendi, D. Akca, H. Topan, An emprical point error model for TLS derived point clouds, ISPRS Arch. XLI-B5 (2016) 557–563, https://doi.org/10.5194/isprs-archives-XLI-B5-557-2016.
[17] X. Chen, G. Zhang, J. Zhang, H. Wu, T. Lu, W. Xuan, An average error ellipsoid model for evaluating precision of point cloud from TLS, J. Ind. Soc. Remote Sens. 44 (2016) 865–873, https://doi.org/10.1007/s12524-016-0563-8.
[18] Z. Du, Z. Wu, J. Yang, Error ellipsoid analysis for the diameter measurement of cylindroid components using a laser radar measurement system, Sensors 16 (5) (2016) 714.
[19] Z. Du, Z. Wu, J. Yang, Point cloud uncertainty analysis for laser radar measurement system based on error ellipsoid model, Opt Laser Eng. 79 (2016) 78–84, https://doi.org/10.1016/j.optlaseng.2015.11.010.
[20] A. Thompson, N. Senin, C. Giusca, R. Leach, Topography of selectively laser melted surfaces: a comparison of different measurement methods, CIRP Ann. 66 (1) (2017) 543–546, https://doi.org/10.1016/j.cirp.2017.04.075.
[21] N. Senin, S. Catalucci, M. Moretti, R.K. Leach, Statistical point cloud model to investigate measurement uncertainty in coordinate metrology, Precis. Eng. 70 (2021) 44–62, https://doi.org/10.1016/j.precisioneng.2021.01.008.
[22] Q. Li, R. Xiong, T. Vidal-Calleja, A GMM based uncertainty model for point clouds registration, Rob. Auton. Syst. 91 (2017) 349–362, https://doi.org/10.1016/j.robot.2016.11.021.
[23] A.B. Forbes, Uncertainty evaluation associated with fitting geometric surfaces to coordinate data, Metrologia 43 (2006) 282–290, https://doi.org/10.1088/0026-1394/43/4/S16.
[24] A.B. Forbes, Surface fitting taking into account uncertainty structure in coordinate data, Meas. Sci. Technol. 17 (2006) 553–558, https://doi.org/10.1088/0957-0233/17/3/S16.
[25] F.A. Maken, F. Ramos, L. Ott, Stein ICP for uncertainty estimation in point cloud matching, IEEE Robot Autom. Lett. 7 (2022) 1063–1070, https://doi.org/10.1109/LRA.2021.3137503.
[26] K.S. Bhandary, N. Hochgeschwender, P. Plöger, F. Kirchner, M. Valdenegro-Toro, Evaluating uncertainty estimation methods on 3D semantic segmentation of point clouds, arXiv e-prints arXiv:2007.01787 (2020), doi: 10.48550/arXiv.2007.01787.
[27] Y. Yang, Y. Jin, M. Price, G. Abdelal, C. Higgins, P. Maropoulos, Investigation of point cloud registration uncertainty for gap measurement of aircraft wing assembly, IEEE 8th Intern. Work. MetroAeroSpace (2021) 164–169, https://doi.org/10.1109/MetroAeroSpace51421.2021.9511727.
[28] D.J. Brus, J.J. de Gruijter, Estimation of non-ergodic variograms and their sampling variance by design-based sampling strategies, Math. Geol. 26 (4) (1994) 437–454, https://doi.org/10.1007/BF02083488.
[29] P.M. Atkinson, C.D. Lloyd, Non-stationary variogram models for geostatistical sampling optimisation: an empirical investigation using elevation data, Comput. Geosci. 33 (2007) 1285–1300, https://doi.org/10.1016/j.cageo.2007.05.011.
[30] R. Webster, M.A. Oliver, A tutorial guide to geostatistics: computing and modelling variograms and kriging, Catena 113 (2014) 56–69, https://doi.org/10.1016/j.catena.2013.09.006.
[31] D. Nychka, D. Hammerling, M. Krock, A. Wiens, Modeling and emulation of nonstationary Gaussian fields, Spat. Stat. 28 (2018) 21–38, https://doi.org/10.1016/j.spasta.2018.08.006.
[32] F. Gerber, D.W. Nychka, Parallel cross-validation: a scalable fitting method for Gaussian process models, Comput. Stat. Data Anal. 155 (2021) 107113, https://doi.org/10.1016/j.csda.2020.107113.
[33] H. Haitjema, Uncertainty in measurement of surface topography, Surf. Topogr. Metrol. Prop. 3 (3) (2015) 035004.
[34] P. Besl, N. McKay, A method for registration of 3-D shapes, IEEE Trans. Pattern Anal. Mach. Intell. 14 (1992) 239–256, https://doi.org/10.1109/34.121791.
[35] S. Rusinkiewicz, M. Levoy, Efficient variants of the ICP algorithm, Proc. Int. Conf. 3-D Digit. Imaging Model. 3DIM (2001) 145–152, https://doi.org/10.1109/IM.2001.924423.
[36] T. Akenine-Möller, E. Haines, N. Hoffman, A. Pesce, M. Iwanicki, S. Hillaire, Real-Time Rendering, CRC Press, Los Angeles, 2018.
[37] J. Elseberg, S. Magnenat, R. Siegwart, N. Andreas, Comparison of nearest-neighbor-search strategies and implementations for efficient shape registration, J. Softw. Eng. Robot. 3 (2012) 2–12, https://doi.org/10.6092/JOSER_2012_03_01_P2.
[38] Y. Chen, A. Wiesel, Y.C. Eldar, A.O. Hero, Shrinkage algorithms for MMSE covariance estimation, IEEE Trans. Signal Process. 58 (2010) 5016–5029, https://doi.org/10.1109/TSP.2010.2053029.
[39] V.M. Rivas Santos, A. Thompson, D. Sims-Waterhouse, I. Maskery, P. Woolliams, R. Leach, Design and characterisation of an additive manufacturing benchmarking artefact following a design-for-metrology approach, Addit. Manuf. 32 (2020) 100964, https://doi.org/10.1016/j.addma.2019.100964.
[40] VDI/VDE 2634 part 3, Optical 3D-Measuring Systems - Multiple View Systems Based on Area Scanning, Verein Deutscher Ingenieure/Verband Der Elektrotechnik Elektronik Informationstechnik, 2008-12 .
[41] M. Pauly, M. Gross, L.P. Kobbelt, Efficient simplification of point-sampled surfaces, Proc. IEEE Vis. (2002) 163–170, https://doi.org/10.1109/VISUAL.2002.1183771.
[42] D. Flack, Measurement Good Practice Guide No. 130 Co-ordinate Measuring Machine Task-Specific Measurement Uncertainties, National Physical Laboratory, London, 2013.
[43] BS ISO 22514 part 7, Statistical Methods in Process Management - Capability and Performance - Part 7: Capability of Measurement Processes, International Organization for Standardization, 2012.
[44] M. van Steen, A.S. Tanenbaum, A brief introduction to distributed systems, Computing 98 (2016) 967–1009, https://doi.org/10.1007/s00607-016-0508-7.